Oxygen Chemisorption, Formation, and Thermal Stability of Pt Oxides on Pt Nanoparticles Supported on SiO₂/Si(001): Size Effects

Luis K. Ono,[†] Jason R. Croy,[†] Helge Heinrich,[†,‡] and Beatriz Roldan Cuenya*[,†]

[†]Department of Physics, and [‡]Advanced Materials Processing and Analysis Center, University of Central Florida, Orlando, Florida 32816, United States

Ⓢ *Supporting Information*

ABSTRACT: The changes induced in the structure and chemical state of size-selected Pt nanoparticles (NPs) supported on ultrathin SiO₂ films upon exposure to oxygen have been investigated by atomic force microscopy (AFM), transmission electron microscopy (TEM), in situ X-ray photoelectron spectroscopy (XPS), and temperature-programmed desorption (TPD). For low atomic oxygen exposures, chemisorbed oxygen species were detected on all samples. Exposure to higher atomic oxygen coverages at room temperature leads to the formation and stabilization of PtO$_x$ species (PtO₂ and PtO). On all samples, a two-step thermal

decomposition process was observed upon annealing in ultrahigh vacuum: PtO₂ → PtO → Pt. For NPs in the 2−6 nm range, the NP size was found to affect the strength of the O binding. Contrary to the case of Pt(111), where no oxides were detected above 700 K, 10−20% PtO was detected on the NP samples via XPS at the same temperature, suggesting the presence of strongly bound oxygen species. In addition, for identical atomic oxygen exposures, decreasing the NP size was found to favor their ability to form oxides. Interestingly, regardless of whether the desorption of chemisorbed oxygen species or that of oxygen in PtO$_x$ species was considered, our TPD data revealed higher O₂-desorption temperatures for the Pt NPs as compared with the Pt(111) surface. Furthermore, a clear size-dependent trend was observed, with an increase in the strength of the oxygen bonding with decreasing NP size.
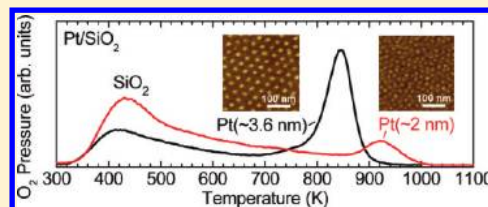
1. INTRODUCTION

The oxidation of Pt is of significant importance both practically and scientifically due to the broad use of this material in industrial catalytic processes for the abatement of automobile exhaust gases in CO oxidation reactions, NO$_x$ reduction, and the combustion of volatile organic compounds.[1] It has been suggested that a number of oxidation reactions involving Pt and other metal surfaces proceed via Mars−van Krevelen processes.[2−5] Reactants are first oxidized by oxygen atoms that are initially present on surface Pt oxides, and the subsequent interaction with gas-phase oxygen reoxidizes Pt, completing the cycle. A thorough understanding of the binding of oxygen, the different stages of oxidation, and the chemical and structural nature of the oxide phases formed on Pt surfaces is crucial for the development of more efficient catalysts for the above reactions. For example, Pt₃O₄ was found to be the active phase for the oxidation of CO and dissociation of CH₄, whereas α-PtO₂ was inactive.[6,7] On the other hand, a correlation between the higher degree of oxidation of small Pt NPs supported Al₂O₃ and the decrease in the rate of NO₂ dissociation was discussed.[8]

The interaction of oxygen with single-crystal Pt surfaces, as for example, Pt(111), Pt(100), and Pt(110), has been studied in detail in the past.[9−18] Gland[12] has shown that oxygen adsorbs molecularly on Pt(111) below ~150 K. At higher temperatures, oxygen dissociates, resulting in a maximum atomic oxygen coverage (θ) of one oxygen atom for every four platinum atoms, that is, θ = 0.25 ML (1 ML$_{Pt(111)}$ = 1.51 × 10^{15} cm^{-2}). A coverage of θ > 0.25 ML cannot be achieved through molecular

adsorption and dissociation, and higher coverages must be obtained by the use of atomic oxygen, ozone (O₃), dissociation of NO₂, or other aggressive treatments.[11,14,19] For oxygen coverages below 0.5 ML, two states corresponding to chemisorbed oxygen in p(2 × 2) and p(2 × 1) structures were reported, whereas for θ > 0.5 ML, oxide chains are observed.[20] These chains have been identified as the precursor to bulk-like PtO₂ on the Pt(111) surface at coverages exceeding 0.75 ML.[20] A maximum oxygen uptake of 2.4 ML on Pt(111) and the formation of PtO$_x$ nanoclusters were observed upon O₃ dosing.[11] The interaction of oxygen with Pt(100) surfaces shows additional unique features, including a higher saturation coverage (0.6−4.5 ML depending on the dosing conditions).[10,21−25] On stepped Pt surfaces (e.g., Pt(110), Pt(210), Pt(211), Pt(335), Pt(411), and Pt(533)), enhanced O₂ dissociation at steps was observed, which facilitates oxidation.[17,26−32] The formation and stability of Pt oxides is especially relevant for fuel cell anodes, where dissolution of Pt has been associated with the initial stages of surface oxide formation.[33] Interestingly, once an oxide layer is formed, further oxidation may proceed rapidly through an autocatalytic process.[34,35] Oxidation generally requires the dissociation of O₂ as a first step, and as discussed above for Pt, this process becomes kinetically limited even at relatively low coverages. However, it has been shown for both Pb and Ru that, once

Table 1. Synthesis Parameters, Average AFM and TEM Heights, and TEM Diameters of Polymer-Free Micellar Pt NPs Supported on SiO_2/Si(001)[a]

sample	molecular weight PS(x), P2VP(y)	metal salt/P2VP ratio (r)	TEM diameter (nm)	TEM height (nm)	AFM height (nm)	
					before TPD	after TPD 913 K
S1	27 700, 4300	0.2	2.0 ± 0.3	2.0 ± 0.3	2.0 ± 0.8	
S2	27 700, 4300	0.6	3.1 ± 0.8	3.0 ± 0.8	3.6 ± 1.0	3.3 ± 0.9
S3	48 500, 70 000	0.3			6.6 ± 1.3	

[a] The AFM measurements were carried out before and after several O_2 TPD cycles up to 913 K, whereas cross-sectional TEM measurements were conducted after annealing in UHV at 1000 K.

oxide formation starts, O_2 dissociation readily happens over PbO and RuO_2.

The understanding of the mechanisms underlying the oxidation of metal NPs presents further unique challenges due to the fact that their surfaces are not as well-defined as those of bulk single crystals. For example, size, coordination of surface atoms, substrate effects, and the presence of different surface facets must be taken into consideration. Under inert atmospheres (e.g., ultrahigh-vacuum (UHV) conditions), Pt NPs present a combination of the two lowest energy surfaces, (111) and (100).[6,36] Therefore, any properties observed are likely a convolution of the properties of these two surfaces. In addition, drastic changes in the morphology and equilibrium shapes of Pt, Pd, and Rh nanocrystals in oxygen environments have been reported,[37−39] with close-packed (111) facets dominating under low O_2 pressures, and nanocrystal rounding occurring at elevated pressures due to the preferential adsorption of oxygen on (110) open surfaces. An increase in the total area of (100) facets at the expense of (111) surfaces was also observed for Rh NPs upon oxidation,[40] and even Au NPs were found to experience shape changes (rounding and substrate dewetting) under oxidizing atmospheres.[41,42] These studies demonstrate that chemisorption-induced morphological changes in NPs need to be considered when models to explain oxidation and catalytic reactivity are proposed. Another complication when dealing with NPs is the control over the NP size, since the activation energy for the dissociation of adsorbed oxygen has been predicted to decrease with decreasing particle size.[43] For other metals (e.g., Au and Pd), a size dependency in the binding of oxygen to NPs has been reported, with stronger binding being generally associated with smaller cluster sizes.[44−46] In addition, the type of oxide that preferentially forms on Pt NPs has been suggested to be affected by the NP size, with PtO_2 being the most stable oxide for NP sizes less than ∼1.3 nm, and PtO for sizes greater than ∼2.0 nm.[47] Calculations of the transition temperature for the decomposition of α-PtO_2 to Pt_3O_4 and Pt also revealed a size dependency.[6,7] Further, the specific shape of Pt NPs was also found to influence their ability to dissociate oxygen.[48]

The above examples reiterate the intrinsic difficulties associated with characterizing the interaction of oxygen with metal NPs and their subsequent oxidation, and the necessity of more in-depth studies targeting model material systems where a strict control of the NP size and shape can be achieved. Furthermore, possible dynamic changes in the structure and chemical state of these NPs under oxidizing environments must be considered. Our work provides insight into the interaction of oxygen with Pt NPs supported on ultrathin SiO_2 films, in particular, the formation and thermal stability of PtO_x species. For this purpose, a

synergistic combination of AFM, TEM, XPS, and TPD was used. The following questions will be addressed: (i) Does the NP size determine its ability to chemisorb oxygen and subsequently form platinum oxides? (ii) Does the NP size influence the final oxidation state of Pt NPs (Pt^{4+} versus Pt^{2+}) for a given coverage/exposure? (iii) Do PtO and PtO_2 species coexist? (iv) Is oxygen, either as a chemisorbed species or in PtO_x compounds, more stable on NPs as compared to bulk single-crystal surfaces? (v) Is the binding of atomic oxygen stronger on NPs or on single-crystal Pt surfaces? (vi) Is there any size dependency?

2. EXPERIMENTAL SECTION

2.1. Nanoparticle Synthesis. Size-selected Pt NPs were obtained by micelle encapsulation using polystyrene-2-vinylpyridine (PS-P2VP) diblock copolymers as described in detail in refs 2 and 49−53. Reverse micelles are formed by dissolving the nonpolar/polar PS-P2VP polymers in toluene (nonpolar). The micelle cores (P2VP) are subsequently loaded with H_2PtCl_6·6 H_2O. The NP size can be tuned by changing the molecular weight of the polymer core (P2VP) or by modifying the metal salt/P2VP ratio. The Pt NPs thus obtained were dip-coated on native-SiO_2/Si(001) substrates. The polymeric shell of the NPs was then removed by an in situ (UHV) O_2-plasma treatment ($P[O_2]$ = 4 × 10^{-5} mbar, 120 min) at room temperature. According to cross-sectional TEM images, the former treatment leads to the formation of an ∼4 nm thick SiO_2 film. Additional prolonged exposures to atomic oxygen during the TPD cycles leads to an increase in the SiO_2 thickness. No impurities were observed in the SiO_2 films grown in situ within the resolution limits of XPS.

Morphological characterization before and after polymer removal was carried out ex situ via AFM (Digital Instruments, Nanoscope III) and TEM (Tecnai F30, 300 kV). Table 1 summarizes the parameters used in the synthesis of our samples as well as the NP size (height and diameter) distributions obtained via AFM and cross-sectional TEM.

In addition to the NP samples, a Pt(111) single crystal was used in the experiments as a bulk Pt reference. The crystal was cleaned by several cycles of Ar^+ sputtering (500 eV, 4 μA, 60 min), annealing in oxygen ($P[O_2]$ = 5 × 10^{-8} mbar) at 800 K for 30 min, and annealing in UHV at 1000 K for 30 min. The process was repeated until no contaminants could be detected by XPS.

2.2. Structural and Chemical Characterization (AFM, TEM, XPS, and TPD). Sample morphology, including average NP size and shape, was extracted from ex situ AFM and cross-sectional TEM images (bright and dark field). The cross-sectional TEM

samples were prepared by a focused ion beam system (FIB, FEI 200TEM).

The chemical composition and oxidation state of our NP samples were investigated in situ in a UHV system (SPECS GmbH) equipped with a monochromatic X-ray source (XR-50M), a hemispherical analyzer (Phoibos 100), and a differentially pumped quadrupole mass spectrometer (QMS, Hiden Analytical, HAL 301/3F) with an electron-bombardment sample heating stage connected to a PID temperature controller (Eurotherm 2048) for TPD experiments. Chemisorbed oxygen species and Pt oxides were obtained by exposing the samples (Pt NPs on $SiO_2/Si(001)$ and Pt(111)) to an in situ O_2 plasma at room temperature (RT). In situ XPS measurements were employed for compositional analysis (i.e., $Pt^{\delta+}$ content). The samples were isochronally annealed from RT to 1000 K for 10 min and subsequently cooled to RT under a flow of liquid nitrogen, after which XPS data were immediately acquired. Sample heating was done following a linear heating ramp ($\beta = 3$ K/s). XPS data were collected using monochromatic X-ray radiation (Al$-$Kα, 1486.6 eV) from a source operating at 350 W. All NP spectra were referenced to the binding energy (BE) of the Si^0 $2p_{3/2}$ peak at 99.3 eV. The ultrathin nature of the SiO_2 support ($\sim$4 nm according to TEM[53]) permitted the detection of the underlying Si substrate via XPS. The fits of the Pt 4f spectra were done after the subtraction of a Shirley background using an asymmetric line-shape-function built into the software CASA XPS.[2] The spectra were fitted with three doublets corresponding to metallic Pt ($4f_{7/2} \sim 71.1$ eV), PtO ($4f_{7/2} \sim 72.3$ eV), and PtO_2 ($4f_{7/2} \sim 73.8$ eV).[54] The maximum width (fwhm) of each component was held constant (± 0.2 eV) [Pt^0 (1.2 eV), PtO (1.7 eV), PtO_2 (1.9 eV)] from spectrum to spectrum for the NP samples. For the Pt(111), the higher intensity of the XPS signal allowed the use of narrower peak widths of $\sim$1.0 eV (Pt^0), $\sim$1.3 eV (Pt^{2+}), and $\sim$1.5 eV (Pt^{4+}). According to the literature,[55,56] the distinction between Pt_3O_4 and PtO_2 species might not be possible solely based on XPS BEs. Because the oxidation state of Pt in Pt_3O_4 is higher than in PtO and lower than in PtO_2, an intermediate BE is expected for this oxide species. Within the resolution of laboratory XPS systems, such a BE is basically indistinguishable from that of PtO_2. Considering that α-PtO_2 has been described to be thermodynamically favored over Pt_3O_4 on Pt(111),[7,19,57] and noting the wide range of BEs reported for the different Pt oxides,[54] we have assigned in the present manuscript the commonly reported PtO and PtO_2 species to the oxides in our samples.[12]

For the TPD experiments, all samples underwent an identical O_2-plasma treatment at RT to generate the initial atomic oxygen coverages. To obtain the TPD spectra, the samples were placed $\sim$3 mm away from the opening of a differentially pumped QMS and heated at a rate of $\beta = 5$ K/s while recording the partial pressure of molecular oxygen ($m/q = 32$).

A maximum heating ramp temperature of 1200 K was used during the TPD measurements for the Pt(111) sample. Preliminary tests revealed irreproducible TPD spectra when consecutive, analogous TPD cycles up to 1200 K were carried out on samples containing small Pt NPs. AFM images from S2 (Table 1) acquired after different TPD cycles (different maximum annealing temperatures and successive TPD ramps; see Figure 1 in the Supporting Information) indicated that the origin of such irreproducible TPD traces was changes in the NP morphology (decrease in the NP height) during heating. To address this issue, multiple identical samples containing small NPs were simultaneously dip-coated into the same Pt NP solution. Subsequently,
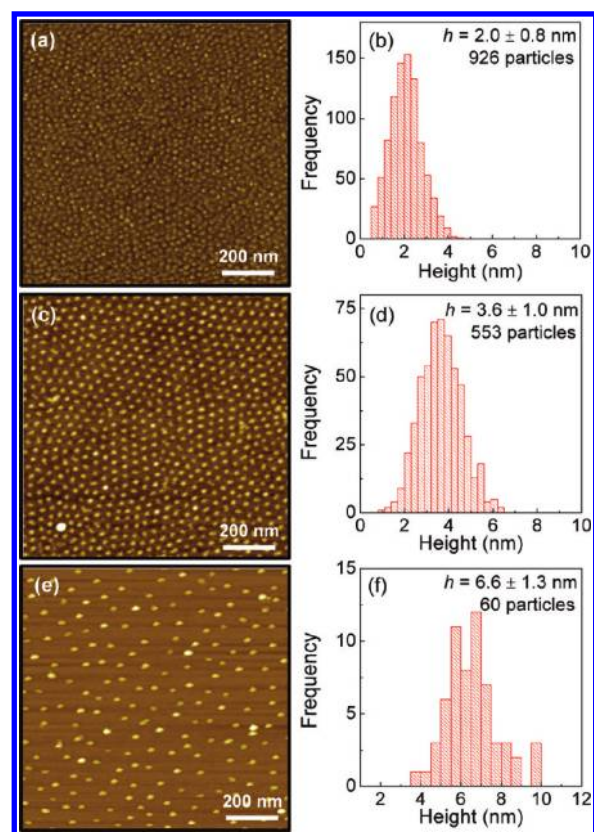
Figure 1. AFM images (a, c, e) and corresponding height distributions (b, d, f) of Pt/SiO_2/Si(001) after removal of the encapsulating polymers. (a, b) S1 (2 nm), (c, d) S2 (3.6 nm), and (e, f) S3 (6.6 nm).

the O_2-coverage dependence was carried out on separate, but identically prepared, fresh samples (S1) with TPD ramps up to 1200 K. Such drastic changes in NP height were not observed for the larger NPs (S2), and therefore, successive O_2 TPD dosings were carried out on the same sample. However, the maximum heating temperature had to be reduced to 913 K for low O_2 coverages to avoid morphological changes. Such a reduction of the maximum annealing temperature during the TPD cycle could not be implemented for the smallest Pt NPs (S1) because higher O_2-desorption temperatures were observed for this sample (peak at $\sim$900 K). Further details on the reproducibility of the TPD experiments can be found in the Supporting Information and Figures 1$-$3 in the Supporting Information.

It should be noted that the sample pretreatments (oxygen dosing) for the two studies described in this work (XPS and TPD) are different. For the XPS study, samples were exposed to long O_2-plasma treatments (2 h, $\sim$216 kL, where 1 Langmuir = 10^{-6} Torr·sec) in order to create completely oxidized particles. After this, isochronal (10 min) annealing treatments from RT to 1000 K were carried out. Subsequently, the decomposition of PtO_x species was monitored by XPS. For the TPD studies, the samples were exposed to different oxygen coverages ranging from 450 L to 216 kL. The chemical state of our TPD samples after each O_2 dosing and before the subsequent TPD measurement was also monitored via XPS. The possible diffusion of Si from the underlying Si substrate through the SiO_2 films ($\geq$4 nm) to the sample surface was considered. A contribution of such effects to the TPD data was ruled out due to the low temperatures ($T < 1100$ K) and short duration (<2 min) of the experiments.

16858

dx.doi.org/10.1021/jp204743q |*J. Phys. Chem. C* 2011, 115, 16856–16866
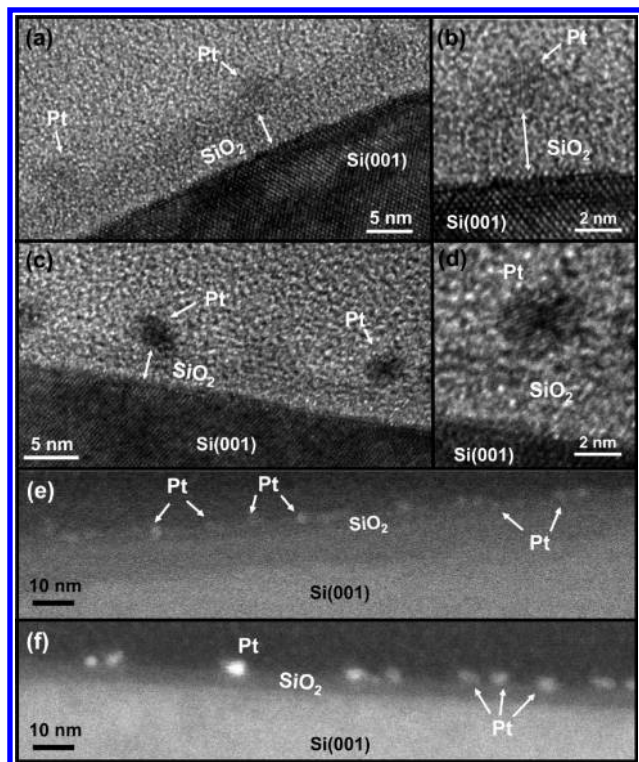
Figure 2. Cross-sectional (a−d) TEM and (e, f) STEM images of micellar Pt NPs supported on SiO$_2$/Si(001) taken after O$_2$ plasma and subsequent annealing from RT to 1000 K in UHV. (a, b, e) S1 and (c, d, f) S2.

3. RESULTS AND DISCUSSION

3.1. Morphological Characterization (AFM, TEM). Figure 1 shows AFM images (a, c, e) and the respective height histograms (b, d, f) of micellar Pt NPs dip-coated on SiO$_2$/Si(001) taken after polymer removal by an O$_2$-plasma treatment. We can see from this figure that the samples exhibit uniform dispersion in both size (monodispersed) and surface coverage. Two polymers with different head and tail sizes were used for the synthesis of these NPs (see Table 1 for details), which leads to the following average interparticle distances: 29 ± 4 nm (S1), 41 ± 7 nm (S2), and 77 ± 15 (S3). In addition, for a polymer with a given head size (P2VP group), the metal-to-polymer ratio (r) was changed from 0.2 to 0.6 (S1 and S2), leading to NPs of different average sizes. The average NP heights extracted from the histograms in Figure 1 are 2.0 ± 0.8 nm for S1, 3.6 ± 1.0 nm for S2, and 6.6 ± 1.3 nm for S3.

Figure 2 displays cross-sectional TEM images of NPs in S1 (a, b, e) and S2 (c, d, f) acquired ex situ after O$_2$-plasma exposure and subsequent annealing in UHV at 1000 K. Nanoparticles with nearly spherical shapes and sizes of ∼2.0 nm (S1) and ∼3.1 nm (S2) were observed. The images shown in (a−d) were acquired in the bright-field mode and (e, f) in high-angle annular dark-field (HAADF) mode. The brightest areas in (e) and (f) correspond to the elements with the highest atomic number (Z-contrast), in this case, to the Pt NPs.

3.2. Formation and Thermal Stability of PtO$_x$ Species (XPS). *3.2.1. Pt(111).* Figure 3 displays XPS spectra from the Pt 4f core-level region of a clean Pt(111) single crystal obtained after exposure to atomic oxygen at RT (O$_2$ plasma) and subsequent annealing in UHV. Reference lines corresponding to the Pt 4f$_{7/2}$ and 4f$_{5/2}$ core levels of Pt metal (solid lines), Pt^{2+} in PtO

Figure 3. XPS spectra from the Pt 4f core-level region of a Pt(111) single crystal obtained at room temperature after O$_2$-plasma exposure (bottom) and subsequent annealing in UHV at the temperatures provided. The vertical lines indicate the positions of the 4f peaks of metallic Pt (solid lines), Pt^{2+} in PtO (dashed lines), and Pt^{4+} in PtO$_2$ (dashed lines) at the energies given in the Experimental Section.

(dashed lines), and Pt^{4+} in PtO$_2$ (dashed lines) are indicated in Figure 3. Directly after in situ oxidation, most of the PtO$_x$ species formed correspond to PtO$_2$, although PtO is also present. Minimum PtO$_x$ decomposition was found to occur below ∼450−500 K. From 500 to 600 K, a steady decrease of the Pt^{4+} component, accompanied by an increase in Pt^{2+} and Pt^0, was observed. This indicates that PtO$_2$ is the least thermally stable PtO$_x$ species, decaying into PtO and subsequently Pt^0. This sequence of stabilities has also been predicted theoretically with α-PtO$_2$ → Pt$_3$O$_4$ → Pt^0 and also follows the reported heats of formation of bulk Pt oxides.[7,58] At temperatures above 600 K, we see an abrupt decomposition of the oxide species and a complete reduction by 700 K. This abrupt change is consistent with reports by Weaver et al.[19] and Saliba et al.[11] suggesting the rapid decomposition, above 700 K, of small PtO$_x$ particles that were formed on Pt(111) surfaces pre-exposed to high oxygen coverages.

16859

dx.doi.org/10.1021/jp204743q |*J. Phys. Chem. C* 2011, 115, 16856–16866
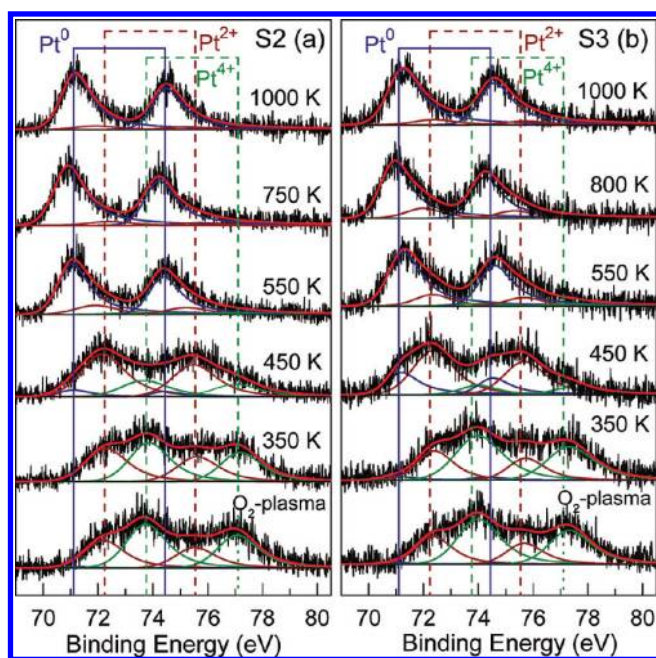
Figure 4. XPS spectra from the Pt 4f core region of Pt NPs supported on SiO₂/Si(001): (a) S2 (3.6 nm) and (b) S3 (6.6 nm), obtained at room temperature after O_2-plasma exposure and subsequent annealing in UHV at the temperatures indicated. The vertical lines indicate the positions of the 4f peaks of metallic Pt (solid lines), Pt^{2+} in PtO (dashed lines), and Pt^{4+} in PtO_2 (dashed lines) at the energies given in the Experimental Section.
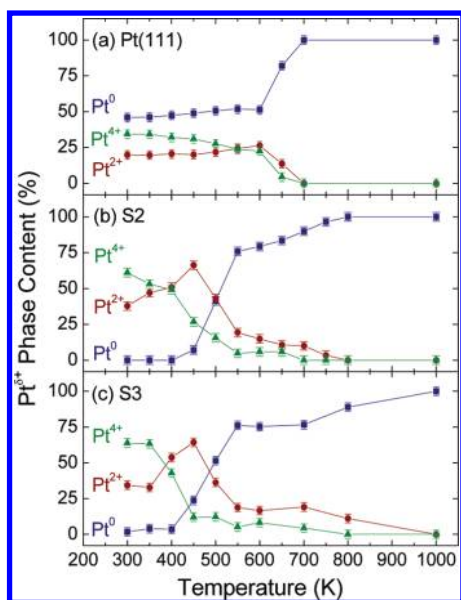
Figure 5. Phase content (%) of Pt oxide species obtained from the analysis of the XPS spectra shown in Figures 3 and 4 after O_2-plasma exposure and subsequent annealing in UHV: (a) Pt(111), (b) S2, and (c) S3.

3.2.2. Pt NPs on SiO₂/Si(001). Figure 4 shows XPS spectra from the Pt 4f core-level region of (a) ~3.6 nm (S2) and (b) ~6.6 nm (S3) Pt NPs supported on SiO₂/Si(001) acquired after an in situ O_2-plasma treatment (bottom) and subsequent isochronal annealing in UHV up to 1000 K. As discussed in the case of Pt(111), for
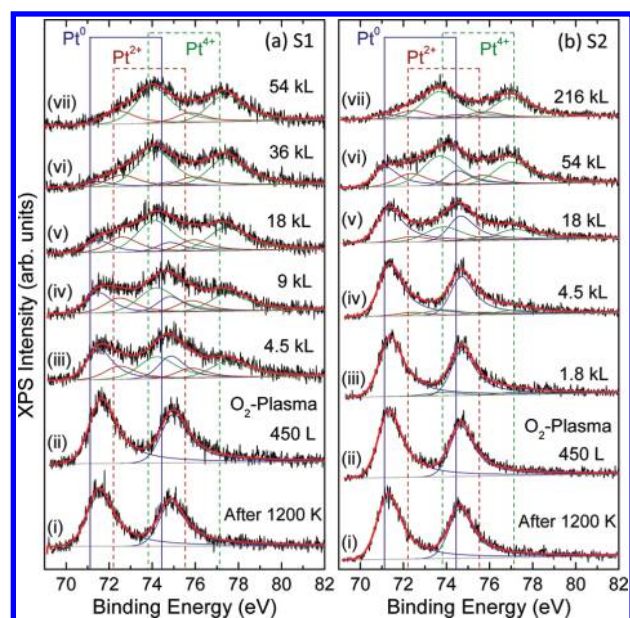
Figure 6. XPS spectra from the Pt 4f core-level region of Pt NPs supported on SiO₂/Si(001): (a) S1 (~2 nm) and (b) S2 (~3.6 nm) obtained (i) after sample annealing at 1200 K in order to decompose surface/subsurface PtO_x and (ii–vii) after subsequent O_2-plasma treatments. The vertical lines indicate the positions of the 4f peaks of metallic Pt (solid lines), Pt^{2+} in PtO (dashed lines), and Pt^{4+} in PtO_2 (dashed lines) at the energies given in the Experimental Section. The different oxygen exposures (O_2 plasma) are given in Langmuir units.

both NP samples, PtO_2 species are mainly formed after prolonged atomic oxygen exposure, and a stepwise decomposition is observed with increasing annealing temperature in UHV ($PtO_2 \rightarrow PtO \rightarrow Pt$ metal). The SiO₂ thin-film support is stable within the temperature range investigated here, and PtSi species, expected to appear at ~73.0 eV for Pt $4f_{7/2}$[59] and ~100.5 eV for Si 2p,[54] are not present (Figure 4, Supporting Information).[53]

Figure 5 shows the phase content of the different Pt species present in the Pt(111) single crystal (a) and Pt NP samples (b) ~3.6 nm (S2) and (c) ~6.6 nm (S3) extracted from the analysis of the Pt 4f XPS spectra in Figures 3 and 4. The NP samples were found to be completely oxidized after the initial O_2-plasma exposure (~70/30 PtO_2/PtO content). The BEs of the three Pt species in the samples containing large Pt NPs (vertical reference lines in Figure 4, S2 and S3) match very closely those of the same species found on bulk Pt(111) (Pt^0, PtO, and PtO_2, Figure 3). This evidences that Pt NPs ≥3.6 nm in size display bulk-like XPS characteristics. In addition, the observed BEs reveal that the Pt NPs do not interact strongly with the ultrathin (~4 nm) SiO₂ support, as was corroborated via TEM, since the NPs initial spherical shape was preserved after annealing. It should be noted that positive BE shifts (+0.4 eV) were observed for the smaller NPs in S1 (2 nm) after PtO_x reduction (Figure 6a, spectrum i), which are assigned to initial and final state effects typical of small metal NPs.[60,61]

Above 400 K, the metallic Pt^0 component appears in the XPS data of the large NP samples (Figure 5), indicating the partial reduction of the Pt oxides. From RT up to 450 K, the content of PtO increases, while that of PtO_2 decreases, and the metallic Pt^0 remains fairly constant (Figure 5b,c). PtO is stable up to 450 K on all samples, and thereafter, the decrease in its signal is accompanied

16860

dx.doi.org/10.1021/jp204743q |*J. Phys. Chem. C* 2011, 115, 16856–16866
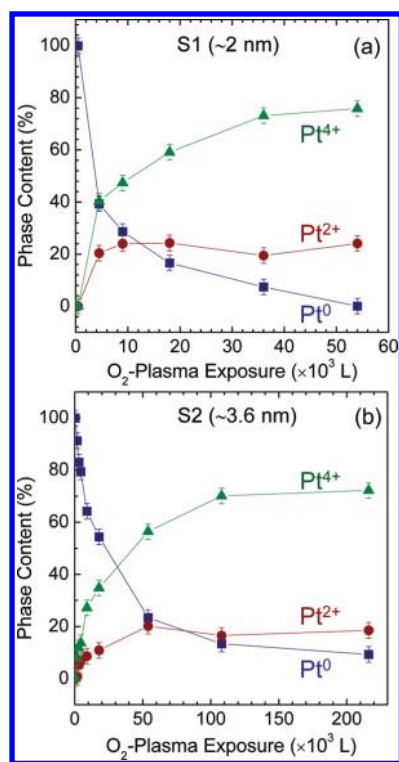
Figure 7. Phase content (%) of Pt oxide species obtained from the analysis of the XPS spectra shown in Figure 6 acquired on micellar Pt NPs after reduction and subsequent exposure to different oxygen coverages (O_2 plasma): (a) S1 and (b) S2.

by an increase in the Pt^0 content. Interestingly, no clear difference in the stability of the PtO_x species was observed when comparing large NPs of different sizes (S2 and S3). In analogy to bulk Pt(111) (Figure 5a), the sequence of oxide decomposition for the NPs follows the path of $PtO_2 \rightarrow PtO \rightarrow Pt^0$. Nevertheless, in contrast with the data obtained for Pt(111), the PtO_2 species formed upon the initial atomic oxygen exposure are clearly less thermally stable than PtO on the Pt NPs. Furthermore, no PtO_x species are observed on Pt(111) above $\sim$700 K, whereas some oxides remain on the NP samples up to $\sim$800 K (Figure 5b,c).

Figure 6 displays XPS data from our TPD samples S1 ($\sim$2 nm) (a) and S2 ($\sim$3.6 nm) (b) acquired after exposure to different atomic oxygen coverages in order to follow the oxidation of the Pt NPs. For reference, XPS spectra of the same samples acquired after reduction at 1200 K are also shown. No $Pt^{\delta+}$ signatures were observed for the lowest O_2-plasma exposures (<4.5 kL) studied, suggesting the presence of chemisorbed oxygen. With increasing atomic oxygen dosing, Pt^{2+} and Pt^{4+} species are detected on both samples. Figure 7 shows the phase content of the distinct Pt species as a function of the RT atomic oxygen exposure (in Langmuir units). In both cases, Pt^0 is converted to PtO and PtO_2, although the oxidation of Pt appears to be more favorable for the smaller NPs (S1), since the maximum content of PtO_x species (nearly complete oxidation) was achieved for a lower total atomic oxygen exposure ($\sim$40 kL for S1 versus $\sim$110 kL for S2). A maximum of $\sim$72−76% PtO_2 and $\sim$19−24% PtO content were observed for these samples.

3.3. Size-Dependent O_2 Desorption (TPD): Pt NPs/SiO$_2$/Si(001). *3.3.1. NP Morphological/Structural Stability.* As described

in the Experimental Section and the Supporting Information (see Figures 1−3 in the Supporting Information), special care must be taken during the acquisition and analysis of TPD data acquired for different oxygen coverages on the same sample. In the case of small Pt NPs, successive O_2 TPD cycles for an identical atomic oxygen coverage lead to irreproducible TPD traces when the maximum annealing temperature exceeds $\sim$913 K (see Figure 1, Supporting Information, for S2). Such an effect is assigned to the desorption of Pt or PtO_x species from our NPs at high temperature. It is well known that small metal NPs have a lower melting temperature than their bulk counterparts. For example, bulk Pt has a melting temperature of $\sim$2040 K, whereas melting temperatures of $\sim$700−800 and 1100−1200 K were calculated for 1.2 and 2.5 nm Pt NPs,[62] and 1720 K for $\sim$4.5 nm NPs.[63] According to those studies, the melting temperature of our $\sim$3.6 nm particles (S2) is estimated to be in the range of $\sim$1200−1700 K. This range is above the 913 K maximum heating ramp temperature used in our study for the investigation of chemisorbed O_2 species on S2. However, as will be shown below, for higher O_2 coverages, more stable oxygen species are found in this sample (PtO_x), and a higher maximum TPD temperature (1200 K) was needed in order to resolve the entire TPD peak (Figure 8d). For the $\sim$2 nm NPs of S1, a maximum heating ramp temperature of 1200 K had to be used, because, for the lowest detectable atomic oxygen dosings, the oxygen-desorption temperatures were in the range of 900−950 K (Figure 8b). In the latter case, a single sample could not be used to investigate different oxygen coverages, because drastic changes in the NP height were observed after each O_2 TPD cycle at 1200 K. The decrease in the NP height observed after multiple TPD cycles above 1000 K is assigned to the formation of volatile Pt oxide species. For example, Wang and Yeh[47] have reported restructuring of Pt crystallites (1−2 nm) to accommodate oxygen accompanied by desorption of PtO_2 and loss of Pt above 750 K.

AFM images and height histograms obtained for sample S2 (two identically prepared, but separate, samples) after 15 O_2 TPD cycles at 913 K (a) and 42 O_2 cycles at 1183 K (b) are shown in Figure 2 (Supporting Information). Height histograms obtained after those treatments indicate the decrease in the NP height from $\sim$3.6 nm before TPD to $\sim$3.3 nm after the treatment at 913 K (c) and to $\sim$2.5 nm after 1183 K (d). These results demonstrate that neither the surface arrangement nor the average NP height are significantly modified upon annealing the O-pre-exposed Pt NPs to 913 K (see Table 1 and Figure 2a,c (Supporting Information)) and that it is acceptable to use a single sample to investigate different oxygen coverages for NPs within this size range (S2).

3.3.2. Size Effects in the Chemisorption of Oxygen and the Decomposition of PtO_x Species. Figure 8 shows O_2 TPD spectra from (a) Pt(111) and (b−d) Pt NPs supported on SiO$_2$/Si(001) acquired after exposure to different atomic oxygen coverages. The data in (b) correspond to S1 ($\sim$2 nm) and those in (c, d) to S2 ($\sim$3.6 nm). Figure 9 summarizes the O_2-desorption temperatures corresponding to the peak maximum in each TPD spectrum of Figure 8b−d as a function of the O_2-plasma exposure.

Following the literature,[10,12,64] the atomic oxygen coverage on Pt(111), generated by exposure to an O_2 plasma, was calibrated by dosing the same surface with molecular oxygen (Figure 8a, open circles). Because only a 0.25 ML saturation coverage can be reached by dosing molecular oxygen onto Pt(111) (desorption peak at $\sim$735 K[11]), the area under that desorption curve can be used to calibrate the coverages obtained upon direct atomic oxygen

16861

dx.doi.org/10.1021/jp204743q |*J. Phys. Chem. C* 2011, 115, 16856−16866
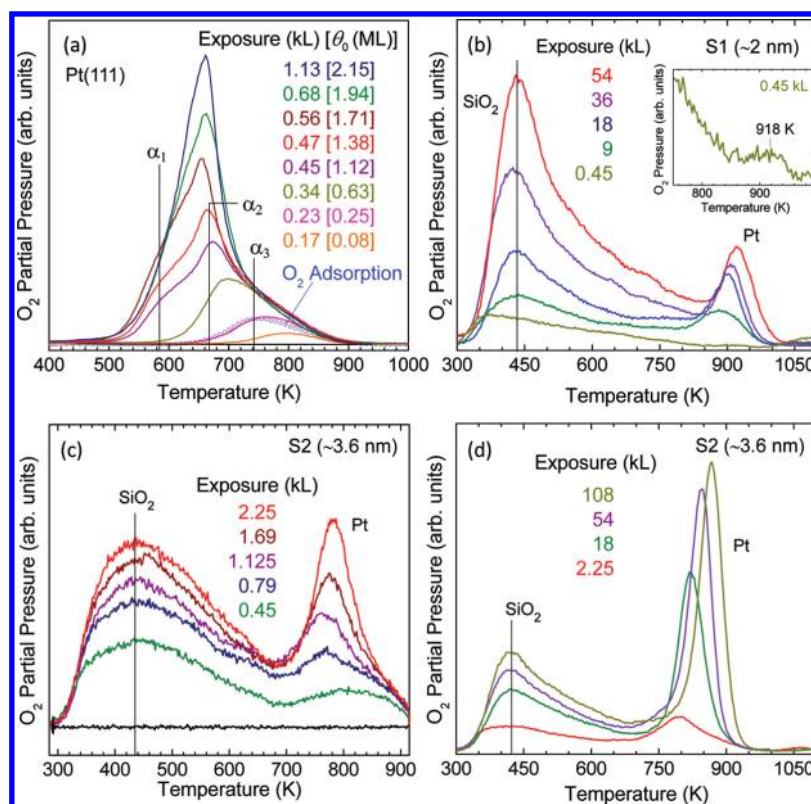
Figure 8. O_2 TPD spectra from (a) Pt(111), (b) S1 ($\sim$2 nm), and (c, d) S2 ($\sim$3.6 nm) Pt NPs supported on SiO_2/Si(001) taken after NP exposure to an O_2 plasma. A linear heating ramp with $\beta = 5$ K/s was used. Several identical samples were used for each distinct oxygen coverage in (b) due to the lack of morphological stability of the small NPs (S1) upon O_2-plasma exposure and subsequent annealing and (d) due to the possibility of having morphological changes in the sample upon the different prolonged exposures to atomic oxygen. The TPD spectra displayed in (c) correspond to different oxygen dosings on the same sample (S2). The initial O_2-plasma exposures are indicated in the plots in Langmuir units as well as in MLs for the Pt(111) single crystal. The open circles in (a) correspond to the oxygen saturation coverage on Pt(111) (0.25 ML) obtained upon molecular oxygen dosing used for coverage calibration purposes. The O_2-plasma exposures are given in Langmuir units.
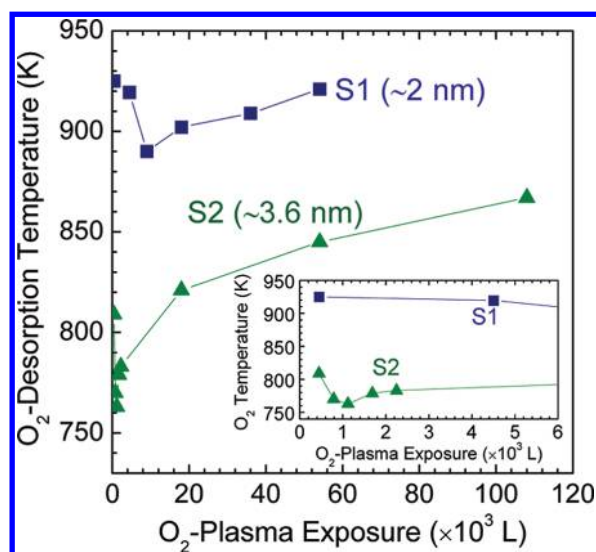
Figure 9. Evolution of the TPD O_2-desorption temperature (peak maximum) with increasing O_2-plasma exposure (in Langmuir units) for samples S1 (squares) and S2 (triangles). The inset shows the dependence upon exposure to low oxygen coverages.

exposure (O_2 plasma). It should be noted that the former calculation assumes a Pt(111) atomic density of 1.51×10^{15} atoms/cm^2,

where a monolayer represents a 1:1 ratio of oxygen to platinum atoms. After this calibration, very similar desorption curves as compared to those reported by Devarajan et al.[20] and Saliba et al.[11] were obtained for our Pt(111) crystal for atomic oxygen coverages of 0.08 ML $< \theta_0 <$ 2.15 ML. Oxygen sequentially populates three different states on the Pt(111) surface. State 3 (α_3) corresponds to an O-(2 $\times$ 2) overlayer and reaches a maximum at $\sim$735 K, at which point state 2 (α_2) begins to appear. On the basis of STM measurements, Weaver's group[20] assigned α_2 to the formation of O-(2 $\times$ 1) domains. At coverages of $\sim$0.4 ML and above, state 1 (α_1) appears at lower temperatures ($\sim$600 K and below), indicating the formation of Pt oxide chains and bulklike PtO_2.[20]

The TPD spectra in (b, d) (Figure 8) correspond to several identically prepared, but separate, Pt NP samples (analogous to S1 and S2, respectively), while (c) corresponds to different oxygen dosings on the same sample (S2). Two characteristic features were observed for all O_2 TPD data collected on SiO_2-supported Pt NP samples. An O_2-desorption peak at $\sim$430 K[46] originating from the SiO_2 substrate, and a second feature at 800–950 K, depending on the oxygen coverage and NP size, is assigned to O_2 desorption from the Pt NPs. For reference, Figure 5 (Supporting Information) displays TPD data from the Pt-free SiO_2/Si(001) substrate after exposure to atomic oxygen. No high-temperature O_2-desorption features were observed for the SiO_2 support, but an increase in the intensity of the 430 K

desorption feature was detected with increasing atomic oxygen coverage. Such weakly bound O species are not associated with the decomposition of the thin oxide support, which is stable in UHV at least up to ~1100 K.[65]

At first glance, a clear size effect in the binding of oxygen to our small and large Pt NPs is observed in Figure 8 as compared to Pt(111). For similar atomic oxygen dosings, overall higher desorption temperatures were obtained for the NP samples. In addition, the highest O_2-desorption temperatures were obtained for the smallest Pt NPs investigated (S1); see Figure 8b. Nevertheless, caution must be taken when comparing the different desorption traces of these three samples, as we have seen that different oxygen species are present on the large and small NPs for the same nominal atomic oxygen exposures. As revealed by the XPS data in Figures 6 and 7, for a given oxygen exposure, for example, 4.5 kL, our smallest NPs (S1) were found to oxidize readily,[66−68] whereas only small amounts of PtO_x species were observed on the larger Pt NPs (S2). On the basis of our XPS data, chemisorbed oxygen species are present in S1 below 4.5 kL O_2-plasma exposure, whereas platinum oxides form for higher atomic oxygen exposures. On the other hand, clear oxidation of the larger NPs (S2) is only observed above 18 kL. Following our XPS data acquired after the different O_2-plasma exposures (Figure 6), the O_2-desorption signals observed for S1 at 900−925 K for coverages ≥ 4.5 kL correspond to the desorption of oxygen from the decomposition of PtO_x species (PtO and PtO_2). Because of the low content of Pt in the latter sample, only weak TPD signals could be measured for lower oxygen dosings (e.g., 0.45 kL, inset in Figure 8b), where, according to XPS, chemisorbed O_2 species are present (before the onset of PtO_x formation). Interestingly, the desorption temperature of chemisorbed oxygen from the NPs in S1 is also higher than that from Pt(111) and the larger NPs in S2. The latter indicates that the stronger O binding to the smallest NPs does not only apply to O in PtO_x species but also to chemisorbed oxygen. This effect is likely related to the enhanced number of low coordinated sites (e.g., kinks, steps) available on the small NPs, where stronger O binding is expected.[69]

The distinction between chemisorbed oxygen and PtO_x species can be more easily made for the larger NPs in S2, since our XPS data indicate the presence of chemisorbed oxygen up to at least 4.5 kL. Figure 8c displays the O_2 TPD data of our large Pt NPs (S2) for a coverage range where no PtO_x species were detected via XPS (≤2.25 kL). Nevertheless, the desorption peak temperatures for all oxygen coverages investigated were found to be larger than those observed for the different chemisorbed oxygen species on Pt(111), with desorption peak temperatures in the range of 760−800 K for S2, as compared with 650−800 K for Pt(111). Analogous to the case of Pt(111), a shift to lower O_2-desorption temperatures (Figure 9) is observed with increasing atomic oxygen coverage on S2 below a total oxygen-plasma exposure of 0.79 kL (Figure 8c). Higher oxygen exposures (Figure 8d) result in a drastic increase in the maximum peak temperature (865 K for 108 kL oxygen exposure for S2), indicating the transition from desorption of chemisorbed O_2 to that of more strongly bound oxygen in PtO_x species. Interestingly, the PtO_x species formed on our small NPs (S1) appear to be more stable than those on the large NPs (S2), since, for a total oxygen exposure of 54 kL, the peak desorption temperature was ~910 K for S1 and ~845 K for S2 (Figure 9). According to XPS, the latter oxygen exposure leads to completely oxidized Pt NPs in S1, while ~23% metallic Pt is still observed in S2.

Furthermore, in addition to the transition from chemisorbed oxygen species to PtO_x, the coverage-dependent trend observed in the desorption temperature of O_2 from our large NPs might also be related to a change in the reaction order. For Pt(111), it has been shown experimentally[11] that oxygen coverages below ~0.3 ML give a reaction order of $n = 2$, whereas for $0.3 < \theta_0 < 1$ ML, n is closer to 1. This implies that the pre-exponential factor and/or the desorption energy are dependent on the coverage. For both NP samples, Figure 8 also reveals an increase in the desorption temperature with increasing oxygen coverage for large oxygen coverages (9−54 kL for S1 and 18−108 kL for S2). Weaver et al.[10] reported previously an analogous trend for Pt(111) (up to 2.9 ML atomic oxygen coverage) and assigned it to explosive oxygen desorption from three-dimensional oxidized clusters. Such explosive desorption is a self-accelerating process occurring at increased desorption rates due to high surface tension present on small cluster. These characteristics re-emphasize the distinction of the two types of oxygen species desorbing from our NPs, with chemisorbed oxygen being present upon low atomic oxygen exposure and PtO_x for high atomic oxygen dosings.

4. FURTHER DISCUSSION

Overall, our TPD data reveal the increase in the strength of the O binding to Pt NPs as compared to bulk Pt(111) either as chemisorbed oxygen or as part of an oxide. Furthermore, a size-dependent trend was observed, with smaller NPs displaying higher oxygen-desorption temperatures. The latter is true when low and high atomic oxygen exposures are considered, indicating that the trend applies to chemisorbed oxygen as well as to PtO_x formed on these samples at room temperature with increasing atomic oxygen exposure.

More specifically, our study reveals the stronger binding of oxygen in PtO_x compounds as compared with the different chemisorbed structures for the large NPs in S2. This distinction is not as clear for the small NPs (S1), because similar O_2-desorption temperatures of ~921−925 K were obtained for chemisorbed oxygen and PtO_x species formed upon exposure to low and high oxygen dosings (0.45 and 54 kL, respectively). When comparing the binding of chemisorbed oxygen on S1 and S2 for the same initial oxygen coverage (0.45 kL), an ~110 K higher O_2-desorption temperature was obtained for the small NPs in S1. Interestingly, higher oxygen binding energies were also observed during the decomposition of PtO_x species from our small NPs. A similar result was previously obtained by our group during the investigation of the stability of Au_2O_3 species on Au NPs supported on SiO_2, with 0.4 eV higher O_2-desorption energies for 1.5 nm Au NPs with respect to 5.0 nm clusters.[46] The former result was corroborated by microkinetic models combined with density functional calculations by Roldán et al.[70] on unsupported Au NPs. However, in the case of Au, only one O_2-desorption state has been commonly identified, even for single-crystal gold surfaces,[71−75] which significantly simplifies the analysis of the TPD spectra. Furthermore, Au does not easily form oxides and the most stable is Au_2O_3, while several stable Pt oxides have been reported (PtO, PtO_2, Pt_3O_4). Putna et al.[44] also reported stronger oxygen binding to small (~2 nm) as compared to large (~9 nm) Pt and Pd NPs evaporated on α-Al_2O_3(0001) upon molecular oxygen exposure at RT. For the same material system, Penner et al.[45] observed an ~200 K higher decomposition temperature of PdO-like species on their Pd NPs as com-

pared with bulk PdO. Moreover, the different structures of the NPs could affect the oxidation and desorption features observed, because they might include Pt(111), Pt(100), and Pt(110) facets,[38] and the relative total fraction of the different facets is expected to depend on the NP size. The latter points are relevant to the interpretation of our results, since Weaver's group[10] has shown that oxygen on Pt(100) is less stable and desorbs at lower temperature than on Pt(111). Even though (111) facets are known to be more stable on small NPs,[76] we cannot rule out the presence of (100) and (110) facets in our samples. In fact, Nolte et al.[40] reported the enhanced stability of (100) facets on large Rh NPs ($d \approx 8$ nm, $h \approx 4.8$ nm) upon exposure to oxygen. Recent calculations also revealed dynamic changes in the structure of Pt NPs under oxidizing environments,[38] including an increase in the fraction of (110) facets. The presence of different facets within the NPs is expected to affect the total oxygen uptake. For example, Pt(100) surfaces have a molecular oxygen uptake nearly twice (0.4 ML) as high as that of Pt(111),[10,11] and an 1.8 ML saturation coverage was reported for Pt(110).[17] Until further detailed information on the geometrical structure of our clusters and its in situ evolution under oxidizing environments is available, only a qualitative discussion of our experimental results is possible. It should be noted that such structural characterization is challenging for oxidized NPs in the 2−4 nm size range.

As was mentioned above, due to the complex nature of supported NPs as compared to single-crystal Pt surfaces, the extraction of quantitative information on different phases of chemisorbed oxygen or oxygen in distinct PtO_x compounds is not possible. First, we have to consider the desorption features originating from the SiO_2 support. In the present case, even though the latter features are well separated in temperature from those of Pt, some residual signal might affect the leading edge regime of the desorption traces of the NP samples, especially in the case of our largest Pt clusters (S2), since they displayed lower maximum desorption temperatures. Second, wider desorption features are observed for the spectral components corresponding to oxygen desorption from Pt in the NP samples as compared to the single-crystal surfaces. This can have different origins: (i) the possible overlap of TPD features corresponding to different oxygen states (at least three reported for chemisorbed oxygen on the Pt(111) surface[20]), (ii) the possibility of having not only (111) facets on the NPs but also (100)[10] and (110),[17,38] and (iii) the finite width of the NP size distribution. Taking the above discussion into consideration, the use of traditional TPD analysis methods, such as the leading edge method, complete analysis, or Arrhenius plots, remains challenging.[10,46,77] The simpler Redhead method is also not suitable for the analysis of these data,[11,77] because it disregards coverage-dependent changes in the desorption order and pre-exponential factor, contrary to the experimental observations of bulk Pt(111).

A saturation in the intensity of the O_2 on Pt TPD peak was observed for the small NPs (S1) for ∼54 kL atomic oxygen exposure, and ∼216 kL for the large NPs (S2) after the subtraction of the SiO_2 background (see Figure 6, Supporting Information). For these saturation oxygen exposures, the small NPs (S1) appear in XPS completely oxidized, whereas ∼9% metallic Pt is still detected on the larger NPs (S2). In both cases, not only PtO_2 but also PtO species are observed. Additionally, Figure 8 and Figure 5 (Supporting Information) reveal that the SiO_2 support film (with and without NPs) appears to act as an oxygen reservoir, since the ∼430 K TPD feature corresponding to O_2 desorbing from SiO_2 continuously increases with

increasing atomic oxygen exposure, never reaching saturation (at least up to a maximum oxygen dosing of 216 kL). The diffusion of atomic or molecular oxygen into amorphous SiO_2 has been investigated in the past.[78−82] Calculations have revealed the incorporation of molecular oxygen inside interstitial voids of SiO_2 without the formation of new Si−O bonds, resulting in low activation energies for diffusion.[78,79] Higher activation energies were obtained for the diffusion of atomic oxygen into SiO_2.[81] Typical energy barriers for the diffusion of oxygen into SiO_2 are in the range of 0.7−1.3 eV, which are similar to the desorption energy obtained here for the ∼430 K TPD peak based on Redhead analysis. The XPS data in Figure 4b (Supporting Information) reveal the increase in the Si^{4+}/Si^0 ratio (spectral areas) with increasing exposure time to atomic oxygen, indicating the growth of the SiO_2 film. This result correlates with the increase in the intensity of the O_2 TPD desorption feature observed for this thin amorphous support film. No changes in the total SiO_2 XPS peak area were observed before and after annealing, indicating the thermal stability of the thin film SiO_2 substrate under the present experimental conditions. Furthermore, exposure of our naturally oxidized Si(001) wafers to the O_2-plasma treatment was found to lead to a negative shift in the BE of the Si^{4+} component (−0.2 eV after 10 kL and −0.3 eV at/above 27 kL, Figure 4a (Supporting Information)) and to peak broadening. The latter effects suggest a change in the chemical environment of the Si^{4+} ions in the thin film support upon O_2-plasma exposure.

The present work highlights the complex nature of the interaction of nanoscale surfaces (metal NPs and ultrathin oxide supports) with oxygen, and the fact that even relatively large NPs (2−3.6 nm) do not behave in the same way as their bulk counterparts, but display stronger oxygen affinity and more stable metal−oxygen bonds.

5. CONCLUSIONS

In summary, we have studied the interaction of oxygen with size-selected Pt NPs supported on SiO_2/Si(001), including the stabilization of chemisorbed oxygen phases and formation of platinum oxides. Our AFM measurements indicated the morphological stability of ∼2−6 nm NPs (NP height and dispersion on the support) upon atomic oxygen exposure and subsequent annealing up to ∼900 K. XPS measurements revealed that small micellar Pt NPs may be fully oxidized by exposure to an oxygen-plasma treatment in UHV at room temperature, although two different PtO_x species were found to coexist (∼76% PtO_2 and ∼24% PtO). After atomic oxygen exposure, three distinct Pt species were found in all samples via XPS, which were assigned to PtO_2 (or Pt_3O_4), PtO, and metallic Pt^0. The thermal decomposition of these oxides goes as $PtO_2 \rightarrow PtO \rightarrow Pt^0$ for all samples, including bulk Pt(111). Although PtO and PtO_2 species coexist up to ∼600 K on the single-crystal sample, the NPs show prompt decomposition of PtO_2 to PtO at lower temperatures (∼350 K). Interestingly, PtO was found to be stable on the NP samples up to ∼800 K.

O_2-desorption spectra reveal that both, small (2 nm) and large (3.6 nm) Pt NPs, show trends similar to the O_2 TPD data from Pt(111), namely, decreasing O_2-desorption temperatures with increasing oxygen coverage for the chemisorbed O_2−desorption regime, and increasing desorption temperatures for the decomposition of PtO_x species. Nevertheless, O_2 desorption from the NPs takes place at higher temperatures as compared

16864

dx.doi.org/10.1021/jp204743q |J. Phys. Chem. C 2011, 115, 16856–16866

with bulk Pt(111) (up to 165 K higher), suggesting stronger O binding to the NPs. In addition, a size dependency was observed, with increasing O_2-desorption temperature with decreasing NP size.

ASSOCIATED CONTENT

Ⓢ Supporting Information. Additional experimental details, information on morphological changes underwent by the Pt NPs upon high-temperature annealing, AFM images and XPS spectra of Pt NPs on SiO_2 after O_2-plasma exposure and different successive O_2 TPD cycles, XPS spectra and TPD data from the $SiO_2/Si(001)$ support after different successive O_2-plasma exposures, and O_2 TPD data from Pt NPs on SiO_2 after subtraction of the SiO_2-related background. This material is available free of charge via the Internet at http://pubs.acs.org.

AUTHOR INFORMATION

Corresponding Author
*E-mail: roldan@ucf.edu.

ACKNOWLEDGMENT

REFERENCES

(1) Bartholomew, C. H.; Farrauto, R. J. *Fundamentals of Industrial Catalytic Processes*; Wiley-Interscience: New York, 2005.

(2) Croy, J. R.; Mostafa, S.; Heinrich, H.; Roldan Cuenya, B. *Catal. Lett.* **2009**, *131*, 21.

(3) Paredis, K.; Ono, L. K.; Mostafa, S.; Li, L.; Zhang, Z.; Yang, J. C.; Barrio, L.; Frenkel, A. I.; Roldan Cuenya, B. *J. Am. Chem. Soc.* **2011**, *133*, 6728.

(4) Meyer, R.; Shaikhutdinov, S. K.; Freund, H. J. *Z. Phys. Chem.* **2004**, *218*, 905.

(5) Alayon, E. M. C.; Singh, J.; Nachtegaal, M.; Harfouche, M.; van Bokhoven, J. A. *J. Catal.* **2009**, *263*, 228.

(6) Seriani, N.; Jin, Z.; Pompe, W.; Ciacchi, L. C. *Phys. Rev. B* **2007**, *76*, 14860.

(7) Seriani, N.; Pompe, W.; Ciacchi, L. C. *J. Phys. Chem. B* **2006**, *110*, 14860.

(8) Olsson, L.; Fridell, E. *J. Catal.* **2002**, *210*, 340.

(9) Parkinson, C. R.; Walker, M.; McConville, C. F. *Surf. Sci.* **2003**, *545*, 19.

(10) Weaver, J. F.; Kan, H. H.; Shumbera, R. B. *J. Phys.: Condens. Matter* **2008**, *20*, 184015.

(11) Saliba, N.; Tsai, Y. L.; Panja, C.; Koel, B. E. *Surf. Sci.* **1999**, *419*, 79.

(12) Gland, J. L. *Surf. Sci.* **1980**, *93*, 487.

(13) Wintterlin, J.; Volkening, S.; Janssens, T. V. W.; Zambelli, T.; Ertl, G. *Science* **1997**, *278*, 1931.

(14) Parker, D. H.; Bartram, M. E.; Koel, B. E. *Surf. Sci.* **1989**, *217*, 489.

(15) Eichler, A.; Mittendorfer, F.; Hafner, J. *Phys. Rev. B* **2000**, *62*, 4744.

(16) Shumbera, R. B.; Kan, H. H.; Weaver, J. F. *J. Phys. Chem. C* **2008**, *112*, 4232.

(17) Li, W. X.; Osterlund, L.; Vestergaard, E. K.; Vang, R. T.; Matthiesen, J.; Pedersen, T. M.; Laegsgaard, E.; Hammer, B.; Besenbacher, F. *Phys. Rev. Lett.* **2004**, *93*, 146104.

(18) Krasnikov, S. A.; Murphy, S.; Berdunov, N.; McCoy, A. P.; Radican, K.; Shvets, I. V. *Nanotechnology* **2010**, *21*, 335301.

(19) Weaver, J. F.; Chen, J. J.; Gerard, A. L. *Surf. Sci.* **2005**, *592*, 83.

(20) Devarajan, S. P.; Hinojosa, J. A.; Weaver, J. F. *Surf. Sci.* **2008**, *602*, 3116.

(21) Liu, D. J.; Evans, J. W. *Chem. Phys. Chem.* **2010**, *11*, 2174.

(22) Behm, R. J.; Thiel, P. A.; Norton, P. R.; Bindner, P. E. *Surf. Sci.* **1984**, *147*, 143.

(23) Barteau, M. A.; Ko, E. I.; Madix, R. J. *Surf. Sci.* **1981**, *102*, 99.

(24) Guo, X. C.; Bradley, J. M.; Hopkinson, A.; King, D. A. *Surf. Sci.* **1994**, *310*, 163.

(25) Norton, P. R.; Griffiths, K.; Bindner, P. E. *Surf. Sci.* **1984**, *138*, 125.

(26) Ducros, R.; Merrill, R. P. *Surf. Sci.* **1976**, *55*, 227.

(27) Sundaram, V. S.; Dawson, P. H. *Surf. Sci.* **1984**, *146*, L593.

(28) McClure, S. M.; Lundwall, M.; Zhou, Z.; Yang, F.; Goodman, D. W. *Catal. Lett.* **2009**, *133*, 298.

(29) Berdau, M.; Moldenhauer, S.; Hammoudeh, A.; Block, J. H.; Christmann, K. *Surf. Sci.* **2000**, *446*, 323.

(30) Fiorin, V.; Borthwick, D.; King, D. A. *Surf. Sci.* **2009**, *603*, 1360.

(31) Wang, H.; Tobin, R. G.; Lambert, D. K.; DiMaggio, C. L.; Fisher, G. B. *Surf. Sci.* **1997**, *372*, 267.

(32) van der Niet, M. J. T. C.; Berg, O. T.; Juurlink, L. B. F.; Koper, M. T. M. *J. Phys. Chem. C* **2010**, *114*, 18953.

(33) Ferreira, P. J.; la O', G. J.; Shao-Horn, Y.; Morgan, D.; Makharia, R.; Kocha, S.; Gasteiger, H. A. *J. Electrochem. Soc.* **2005**, *152*, A2256.

(34) Over, H.; Seitsonen, A. P. *Science* **2002**, *297*, 2003.

(35) Thurmer, K.; Williams, E.; Reutt-Robey, J. *Science* **2002**, *297*, 2033.

(36) Arenz, M.; Mayrhofer, K. J. J.; Stamenkovic, V.; Blizanac, B. B.; Tomoyuki, T.; Ross, P. N.; Markovic, N. M. *J. Am. Chem. Soc.* **2005**, *127*, 6819.

(37) Mittendorfer, F.; Seriani, N.; Dubay, O.; Kresse, G. *Phys. Rev. B* **2007**, *76*, 233413.

(38) Seriani, N.; Mittendorfer, F. *J. Phys.: Condens. Matter* **2008**, *20*, 184023.

(39) Xiao, L.; Schneider, W. F. *Chem. Phys. Lett.* **2010**, *484*, 231.

(40) Nolte, P.; Stierle, A.; Jin-Phillipp, N. Y.; Kasper, N.; Schulli, T. U.; Dosch, H. *Science* **2008**, *321*, 1654.

(41) Giorgio, S.; Cabie, M.; Henry, C. R. *Gold Bull.* **2008**, *41*, 167.

(42) Giorgio, S.; Sao Joao, S.; Nitsche, S.; Chaudenson, D.; Sitja, G.; Henry, C. R. *Ultramicroscopy* **2006**, *106*, 503.

(43) Li, T.; Balbuena, P. B. *J. Phys. Chem. B* **2001**, *105*, 9943.

(44) Putna, E. S.; Vohs, J. M.; Gorte, R. J. *Surf. Sci.* **1997**, *391*, L1178.

(45) Penner, S.; Bera, P.; Pedersen, S.; Ngo, L. T.; Harris, J. J. W.; Campbell, C. T. *J. Phys. Chem. B* **2006**, *110*, 24577.

(46) Ono, L. K.; Roldan Cuenya, B. *J. Phys. Chem. C* **2008**, *112*, 18543.

(47) Wang, C. B.; Yeh, C. T. *J. Catal.* **1998**, *178*, 450.

(48) Mostafa, S.; Behafarid, F.; Croy, J. R.; Ono, L. K.; Li, L.; Yang, J. C.; Frenkel, A. I.; Cuenya, B. R. *J. Am. Chem. Soc.* **2010**, *132*, 15714.

(49) Croy, J. R.; Mostafa, S.; Hickman, L.; Heinrich, H.; Roldan Cuenya, B. *Appl. Catal., A* **2008**, *350*, 207.

(50) Croy, J. R.; Mostafa, S.; Liu, J.; Sohn, Y. H.; Heinrich, H.; Roldan Cuenya, B. *Catal. Lett.* **2007**, *119*, 209.

(51) Croy, J. R.; Mostafa, S.; Liu, J.; Sohn, Y. H.; Roldan Cuenya, B. *Catal. Lett.* **2007**, *118*, 1.

(52) Naitabdi, A.; Behafarid, F.; Cuenya, B. R. *Appl. Phys. Lett.* **2009**, *94*, 083102.

(53) Ono, L. K.; Yuan, B.; Heinrich, H.; Cuenya, B. R. *J. Phys. Chem. C* **2010**, *114*, 22119.

(54) X-ray Photoelectron Spectroscopy Database, Version 3.4 (Web Version), http://srdata.nist.gov/xps/index.htm.

(55) Kuribayashi, K.; Kitamura, S. *Thin Solid Films* **2001**, *400*, 160.

(56) Shumbera, R. B.; Kan, H. H.; Weaver, J. F. *Surf. Sci.* **2007**, *601*, 235.

(57) Samsonov, G. V. *The Oxide Handbook*, 2nd ed.; Plenum Publishing Corporation: New York, 1982.

16865

dx.doi.org/10.1021/jp204743q |*J. Phys. Chem. C* 2011, 115, 16856–16866

(58) Wang, C. B.; Lin, H. K.; Hsu, S. N.; Huang, T. H.; Chiu, H. C. *J. Mol. Catal. A* **2002**, *188*, 201.

(59) Grunthaner, P. J.; Grunthaner, F. J.; Madhukar, A. *J. Vac. Sci. Technol.* **1982**, *20*, 680.

(60) Mason, M. G. *Phys. Rev. B* **1983**, *27*, 748.

(61) Wertheim, G. K.; Dicenzo, S. B.; Youngquist, S. E. *Phys. Rev. Lett.* **1983**, *51*, 2310.

(62) Morrow, B. H.; Striolo, A. *Nanotechnology* **2008**, *19*, 195711.

(63) Wen, Y. H.; Fang, H.; Zhu, Z. Z.; Sun, S. G. *Phys. Lett. A* **2009**, *373*, 272.

(64) Campbell, C. T.; Ertl, G.; Kuipers, H.; Segner, J. *Surf. Sci.* **1981**, *107*, 220.

(65) Koshizaki, N.; Umehara, H.; Oyama, T. *Thin Solid Films* **1998**, *325*, 130.

(66) Han, B. C.; Miranda, C. R.; Ceder, G. *Phys. Rev. B* **2008**, *77*, 075410.

(67) Xu, Y.; Shelton, W. A.; Schneider, W. F. *J. Phys. Chem. A* **2006**, *110*, 5839.

(68) Schalow, T.; Brandt, B.; Starr, D. E.; Laurin, M.; Shaikhutdinov, S. K.; Schauermann, S.; Libuda, J.; Freund, H. J. *Angew. Chem., Int. Ed.* **2006**, *45*, 3693.

(69) Gambardella, P.; Sljivancanin, Z.; Hammer, B.; Blanc, M.; Kuhnke, K.; Kern, K. *Phys. Rev. Lett.* **2001**, *87*, 056103.

(70) Roldan, A.; Novell, G.; Ricart, J. M.; Illas, F. *J. Phys. Chem. C* **2010**, *114*, 5101.

(71) Saliba, N.; Parker, D. H.; Koel, B. E. *Surf. Sci.* **1998**, *410*, 270.

(72) Bondzie, V. A.; Parker, S. C.; Campbell, C. T. *Catal. Lett.* **1999**, *63*, 143.

(73) Choi, K. H.; Coh, B. Y.; Lee, H. I. *Catal. Today* **1998**, *44*, 205.

(74) Gottfried, J. M.; Schmidt, K. J.; Schroeder, S. L. M.; Christmann, K. *Surf. Sci.* **2003**, *525*, 184.

(75) Deng, X. Y.; Min, B. K.; Guloy, A.; Friend, C. M. *J. Am. Chem. Soc.* **2005**, *127*, 9267.

(76) Roldan Cuenya, B.; Croy, J. R.; Mostafa, S.; Behafarid, F.; Li, L.; Zhang, Z.; Yang, J. C.; Wang, Q.; Frenkel, A. I. *J. Am. Chem. Soc.* **2010**, *132*, 8747.

(77) Redhead, P. A. *Vacuum* **1962**, *12*, 203.

(78) Bongiorno, A.; Pasquarello, A. *Phys. Rev. Lett.* **2002**, *88*, 125901.

(79) Chelikowsky, J. R.; Chadi, D. J.; Binggeli, N. *Phys. Rev. B* **2000**, *62*, R2251.

(80) Kajihara, K.; Miura, T.; Kamioka, H.; Aiba, A.; Urarnoto, M.; Morinioto, Y.; Hirano, M.; Skuja, L.; Hosono, H. *J. Non-Cryst. Solids* **2008**, *354*, 224.

(81) Hamann, D. R. *Phys. Rev. Lett.* **1998**, *81*, 3447.

(82) Hoshino, T.; Hata, M.; Neya, S.; Nishioka, Y.; Watanabe, T.; Tatsumura, K.; Ohdomari, L. *Jpn. J. Appl. Phys.* **2003**, *42*, 3560.